Graphite recovery and synthesis of graphene oxide from end-of-life Li-ion batteries: Impact of thermal, mechanical, and mechanochemical pretreatments

Pier Giorgio Schiavi [a,*], Ludovica D'Annibale [a], Andrea Giacomo Marrani [a,**], Francesco Amato [a], Olga Russina [a], Silvia Iacobelli [a], Francesco Mura [b,c], Raphael Sieweck [d], Francesca Pagnanelli [a], Pietro Altimari [a]

[a] Department of Chemistry, Sapienza University of Rome, Piazzale Aldo Moro 5, 00185, Rome, Italy
[b] Department of Basic and Applied Sciences for Engineering, Sapienza University of Rome, Via A. Scarpa 14, 00161, Rome, Italy
[c] Research Centre for Nanotechnology Applied to Engineering, Sapienza University of Rome, Piazzale Aldo Moro 5, 00185, Rome, Italy
[d] Karlsruhe Institute of Technology (KIT), Institute for Applied Materials (IAM), Hermann-von-Helmholtz-Platz 1, Eggenstein-Leopoldshafen, D-76344, Karlsruhe, Germany

A B S T R A C T

This study investigates how common pretreatments for recovering black mass from end-of-life (EoL) electric vehicle (EV) lithium-ion batteries (LIBs) influence graphene oxide (GO) synthesis. Black mass was obtained through (i) industrial-scale carbothermal reduction of whole EV battery packs, (ii) industrial-scale mechanical processing, and (iii) lab-scale mechanochemical treatment via reactive ball milling. Characterizations assessed the impact of these pretreatments, along with conventional acid leaching, on graphite properties such as interlayer spacing, oxidation degree, and defectivity—key factors for potential anode reuse. The mechanochemically treated sample achieved an outstanding GO yield of 92 %, whereas other black masses reached up to 30 %. GO yields were further analysed using the Hummers' method after acid leaching for metal removal. This approach enhanced yields, reaching 96 % for the mechanochemically treated sample and up to 46 % for the others. The improvements were attributed to reduced reagent consumption and the partial exfoliation and oxidation of graphite during leaching. Additionally, lithium intercalation/deintercalation during battery cycling increased GO yield compared to commercial pristine graphite. These findings highlight mechanochemical pretreatment as a promising strategy to integrate high-yield GO production into LIB recycling workflows.

1. Introduction

Effective LIB recycling processes are essential to mitigate environmental issues caused by improper disposal and to recover valuable materials for producing new batteries. Over recent years, numerous recycling methods have been developed, with two primary approaches dominating the field: pyrometallurgical and hydrometallurgical processes. Among these methods, the hydrometallurgical approach stands out as more effective for material recovery, offering the potential to reclaim nearly all battery components while being more energy-efficient than pyrometallurgy. In hydrometallurgical recycling, leaching serves as the core step, playing a pivotal role in the extraction of critical materials [1]. However, the very initial step of any hydrometallurgical recycling process is the pretreatment of LIBs to recover the electrode powder, commonly referred to as "black mass". This powder contains the key materials to be recovered, including metals from the cathode and the graphite from the anode. The most common EoL LIB pretreatments for hydrometallurgical processes include (i) physical-mechanical methods, such as crushing (performed under an inert atmosphere if the batteries are not safely discharged), sieving, magnetic separation, electrostatic separation, and flotation, and (ii) thermal pretreatments, usually conducted at low temperatures when the goal is to recover black mass for subsequent hydrometallurgical processing [2]. This thermal treatment typically involves carbothermal reduction of metals composing the cathode materials, leading to the formation of water-soluble species of lithium that can be easily recovered by water leaching [3–5]. The same recovery mechanism can be supported by mechanochemical pretreatment involving ball milling of the black mass in presence of a reducing agent [6,7].

These pretreatment steps, along with the subsequent refining processes required to recover metals as battery-grade materials, often entail significant energy and reagent consumption, which can limit the

---

economic feasibility of recycling process. Restructuring the recycling process to enable the production of high-value-added materials can mitigate this issue. In this context, numerous studies have explored the development of high-value-added materials derived from the metals in the cathodes of EoL LIBs, enabling wide-ranging applications in energy storage, catalysis, and sensing [8]. However, the graphite in anode materials is often overlooked in LIB recycling approaches, despite its significant potential for recovery and reuse [9]. Additionally, EoL graphite can serve as a valuable source for the production of graphene-based nanomaterials [10]. Graphene is renowned for its exceptional properties, including high electrical and thermal conductivity, remarkable mechanical strength, and flexibility. These characteristics have made graphene a subject of intense research, leading to its exploration in various applications such as energy storage devices, sensors, and advanced electronics. The primary methods for synthesizing graphene include chemical vapor deposition (CVD), liquid-phase exfoliation, chemical reduction of graphene oxide and mechanical exfoliation using ball milling or shear mixing [11]. In order to integrate graphene production from the recycling of LIBs, the production of graphene oxide by the so-called Hummers' method and the subsequent chemical reduction to graphene appears to be the most suitable approach. The process involves the oxidation of graphite to graphite oxide, the exfoliation of graphite oxide, and the subsequent chemical reduction of graphite oxide (GO) to reduced graphene oxide (rGO).

Compared to the other methods mentioned, the Hummers' method uses concentrated sulfuric acid and hydrogen peroxide, which are the reagents typically employed in the leaching of black mass in hydrometallurgical recycling processes [1]. This suggests that treatment of the black mass with the Hummers' method could enable the simultaneous production of graphite oxide and metal leaching [12], a process not feasible with other methods.

Notably, graphite oxidation can occur already during the thermal pretreatment of LIBs to obtain black mass, while exfoliation can be induced through mechanochemical pretreatment, such as ball milling, thus influencing the graphene production when graphite from EoL LIBs is used. Since 2016, studies on the synthesis of graphene from graphite recovered from EoL LIBs have started to appear in the literature. However, only a few existing studies utilize black mass derived from mechanical treatments at an industrial scale as starting material [12,13], while many of the studies focus on the synthesis of GO using graphite manually recovered and manually separated from spent batteries at the lab scale [14–24]. This way, almost pure graphite is obtained and used in the experiments, thus overlooking the influence of the other components that are invariably present in the black mass recovered by pretreatment of LIBs at industrial scale. In addition, the impact of pretreatment methods on GO production has not been reported yet.

In this paper, for the first time, the impact of the pretreatments commonly applied to recover the black mass from EoL LIBs is evaluated in terms of GO yield achieved by the application of the Hummers' method. Industrial-scale thermal pretreatments, including carbothermal reduction of whole battery packs, and industrial-scale mechanical treatments, involving shredding and sieving of EoL LIBs, were assessed. Furthermore, a lab-scale mechano-chemical treatment including the ball milling of the black mass in presence of a reducing agent, was considered reflecting its emerging applications and increasing diffusion in the literature. A detailed experimental analysis was carried out to investigate how different pretreatment methods influence the GO yield. Furthermore, since the black mass contains metals primarily derived from cathode materials, their impact on GO production was carefully analysed after metal removal through conventional acid leaching. This study provided valuable insights into the role of metal content, emphasizing the critical interactions between metal removal, acid leaching commonly applied in hydrometallurgical recycling processes and EoL LIB pretreatments on the overall yield of graphene oxide.

2. Experimental section

Fig. 1 provides a schematic representation of the procedure used to synthesize graphene oxide from black masses obtained through three different pretreatment processes. The experimental procedure follows two distinct routes for the synthesis of GO. In route 1, the Hummers' method is directly applied to the thermally treated (TT), mechanically treated (MT), and mechanochemically treated (MCT) black masses, yielding the corresponding GO samples, named TTH, MTH, and MCTH. In route 2, a conventional acid leaching process is first performed on the TT, MT, and MCT black masses to remove metals. The Hummers' method is then applied, producing the corresponding GO samples, named TTLH, MTLH, and MCTLH.

2.1. Black masses

Thermally treated black mass (TT) was supplied by Accurec Recycling GmbH (Germany). This material was prepared by processing EoL LIB electric vehicle (EV) packs between 480 and 520 °C. The atmosphere was inert (N_2) and the pyrolysis pressure was 800 mbar. After thermal treatment, the batteries were crushed and sieved to recover the corresponding black mass. Mechanically treated black mass (MT) was provided by SK TES (Singapore) and obtained through their proprietary mechanical pretreatment technology. Mechanochemically pretreated black mass (MCT) was prepared by treating the MT black mass using the following protocol. A 65 mL hardened steel vial was equipped with two large steel balls (12.7 mm diameter) and four small steel balls (6.35 mm diameter). Under an argon atmosphere inside a glovebox, 1.47 g of MT black mass and 0.57 g of freshly cut Ca turnings (99.5 %, Alfa Aesar) were added, ensuring a ball-to-sample mass ratio of 10 and a molar ratio of NMC ($LiNi_aMn_bCo_cO_2$) in the black mass to Ca of approximately 2.1. Milling was conducted using a SPEX 8000 shaker mill with three cycles of 1-h milling followed by 15-min rest periods. The as-milled powder was further processed in a glass filter reactor containing 1.5 L of deionized (DI) water, which was stirred mechanically at 500 rpm. A total of 27.8 g of the combined as-milled powder was incrementally added within 10 min using a powder doser, ensuring the safe release of any hydrogen gas generated during the process. After stirring for 30 min at room temperature, the suspension was filtered using suction. The solid residue was resuspended in 1.5 L of DI water, stirred for 30 min, and filtered again. This washing step was repeated twice to ensure thorough cleaning. Finally, the solid was dried in an oven at 80 °C. Black mass metal compositions were estimated by inductively coupled plasma emission spectroscopy (ICP, Avio 220 MAX PerkinElmer Inc.) after microwave assisted digestion (Milestone ETHOS 900 – Milestone srl) of 12 samples of 0.25 g in 4 mL HCl (37 % VWR Chemicals), 4 mL HNO3 (65 %, Carlo Erba Reagents), and 2 mL H_2O_2 (30 %, Sigma-Aldrich). Black mass composition is reported in Table S1.

2.2. Hummers' method

The black masses (TT, MT, MCT) and commercial graphite (natural powder, ≥99.9995 % metals basis, 2–15 μm, Thermo Scientific) were processed using Hummers' method to produce graphene oxide (GO) [1]. The reaction was conducted in a thermostatically controlled jacketed reactor. For each experiment, an amount of black mass containing 3.0 g of graphite was treated with 1.5 g of NaNO3 (AnalR NORMAPUR, VWR Chemicals) and 69 mL of concentrated H_2SO_4 (95 %, VWR Chemicals) as the etching agent. Subsequently, 9.0 g of KMnO4 (99 %, Sigma Aldrich) were added gradually to maintain the reaction temperature below 20 °C, as the reaction between KMnO4 and the acid is highly exothermic. During this stage, the solution began to exhibit a dark brown or green colour due to the formation of the MnO_3^+ compound [2]. The reaction mixture was then heated to 35 °C and maintained at this temperature for 30 min before 138 mL of distilled water was added. The temperature was subsequently increased to 98 °C for 15 min, followed by the addition of
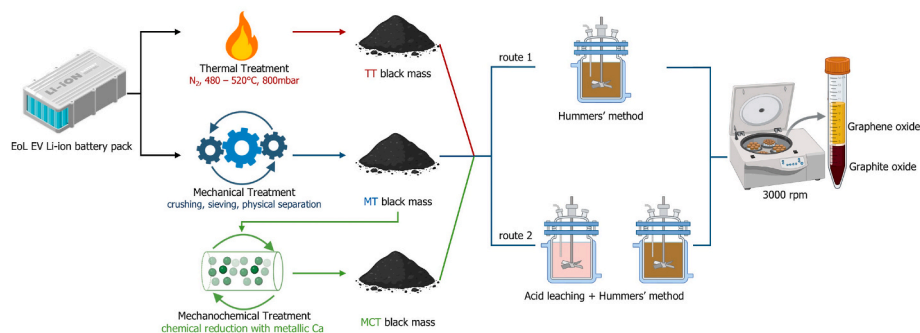
Fig. 1. Schematic of GO synthesis procedure starting from the different black masses.

420 mL of distilled water and 5 mL of H_2O_2, (30 % wt, VWR Chemicals) as a reducing agent. The resulting suspension was subjected to washing by centrifugation five times, each for 30 min at 4000 rpm. For the first wash, 1.12 M HCl (37 %, VWR) was used, while subsequent washes employed distilled water. The first washing solution was collected, brought to a known volume, and analysed using ICP. After each centrifugation step, the supernatant was discarded, and the solid residue was transferred to a beaker and stirred magnetically overnight. The suspension was then sonicated and centrifuged once at 3000 rpm for 40 min. This final centrifugation step separated the supernatant (containing GO) from the sedimented solid residue (comprising graphite oxide). Both the supernatant and the sedimented solid residue were freeze-dried and weighed. The same procedure was applied to commercial graphite and to black masses from which metals had been removed using conventional acid leaching, as described in the following section. The yield of graphene oxide was calculated using the following equation:

$$GO\ yield = \frac{GO\ [g]}{GO[g] + graphite\ oxide[g]} \times 100 \tag{1}$$

2.3. Leaching process

Leaching was performed using 1.5 M H_2SO_4 (95 %, VWR Chemicals) and H_2O_2 (30 % wt, VWR Chemicals) as the reducing agent. The reaction was carried out under mechanical stirring in a thermostatically controlled jacketed reactor. A total of 10 g of black mass was introduced into the reactor along with 100 mL of 1.5 M H_2SO_4. The suspension was heated to 85 °C, the operating temperature for the leaching process. After 1 h, H_2O_2 (30 % wt, VWR Chemicals) was added in an amount equivalent to 15 % by volume of the solution, and the reaction was allowed to proceed for an additional 2 h. Upon completion, vacuum filtration was performed using a rotary pump. The resulting solution was analysed using ICP to quantify the metal extraction yields. The solid residue was thoroughly washed with distilled water until neutrality was achieved and then dried in an oven at 60 °C overnight. The dried residue was weighed the following day. The same procedure was repeated for commercial graphite to assess the potential influence of acid leaching on the GO yield.

2.4. Physicochemical characterizations

Phase composition was investigated through X-ray diffractometer (XRD, Bruker D8 ADVANCE) with a molybdenum anode (Kα = 0.709319 Å), scanning the 2theta range between 4° and 45°. The diffraction data were collected at ambient conditions in Brentano Bragg geometry, depositing the powder samples on a quartz plate. To facilitate the comparison of the experimental data with the literature, they were converted with respect to a Cu radiation with Kα = 1.54056 Å. The interlayer spacing of the (002) graphite plane (d_{002}) was calculated using Bragg's law:

$$d_{002} = \lambda/2\ sin\ \theta \tag{2}$$

Where λ is the wavelength of the X-ray and θ denotes the X-ray diffraction angle. Raman spectra were collected at room temperature in backscattering geometry with an inVia Renishaw micro-Raman spectrometer equipped with an air-cooled CCD detector and super-Notch filters. An Ar^+ ion laser (λ_{laser} = 514 nm) was used, coupled to a Leica DLML microscope with a 20 × objective. The resolution was 2 cm^{-1} and spectra were calibrated using the 520.5 cm^{-1} line of a silicon wafer. Raman spectra were acquired in several different spots on the surface of the samples and each spectrum was acquired with 1 % of power, 10 s of spectral acquisition, and 20 scans. For XPS spectroscopy the water-insoluble powder samples were spread onto a conductive double-sided scotch tape attached to the XPS sample holder. All the water-soluble samples were deposited onto a freshly prepared H-terminated Si(100) surface, used as a support for the drop-casting of 50 µL of a 0.06 mg/mL graphene derivative aqueous dispersion. XPS measurements were carried out using a modified Omicron NanoTechnology MXPS system equipped with monochromatic and achromatic Al Kα (hν = 1486.7 eV) X-ray sources (Omicron XM-1000 and DAR400, respectively), operating the anode at 14 kV and 16 mA. The C 1s photoionization region was acquired using an analyzer pass energy of 20 eV, while the survey spectra were acquired with a pass energy of 50 eV. A take-off angle of 21° with respect to the sample surface normal was adopted. The experimental spectra were theoretically reconstructed using the RxpsG open software [3]. The secondary electrons' background was fitted to a Shirley function and the elastic peaks to pseudo–Voigt functions. The oxygen content was determined through the $R_{O/C}$ ratio obtained after the curve-fitting of the C 1s region, by means of the following formula [4]:

$$R_{O/C} = \frac{P_{C-OH} + 1/2P_{Epoxide} + P_{C=O} + 2P_{COOH}}{P_{gr} + P_{C=C} + P_{C-OH} + P_{Epoxide} + P_{C=O} + P_{COOH}} \tag{3}$$

where the P_x terms represent the OFG peak areas obtained by curve fitting. This formula allows to rule out the possible contributions to the oxygen content of the graphene derived material deriving from black mass components and support material (Si). The relative percentage of the different oxygenated functional groups (uncertainty of ±10 %) was determined using the P_x terms, according to the following equation:

$$P\%_{OFG} = \frac{P_x}{P_{gr} + P_{C=C} + P_{C-OH} + 1/2P_{Epoxide} + P_{C=O} + P_{COOH}} \times 100 \tag{4}$$

TEM imaging and electron diffraction was performed using a JEOL F200 at 200 keV equipped with a Gatan Rio16 CMOS camera, while the EDX mapping has been obtained operating in STEM mode. The particle size distribution was measured by laser scattering on a LA-950 device (Horiba GmbH). About 150 mg of the sample were suspended in iso-propanol and sonicated for 1 min using a SONOPULS HD2200.2 (Bandelin GmbH) before being added dropwise in the LA-950 until a transmission of around 85 % was reached.

3. Results and discussion

3.1. Black mass characterizations

The XRD patterns of the TT sample (Fig. 2a) and the MCT sample (Fig. 2c) indicate the reduction of metals contained in the battery cathode materials. For the TT sample, the XRD pattern reveals a mixture of Co, Ni and Mn in reduced form. The absence of diffraction signals associated with the crystal structure of any lithiated metal oxides (battery cathode materials) suggests the effectiveness of the thermal pretreatment. The thermal pretreatment was conducted between 480 and 520 °C under a nitrogen atmosphere and in the presence of carbon sources, such as those contained in LIBs, leading to carbothermal reduction [5,25]. Similarly, for the MCT sample, the XRD patterns of Co, Ni, and Mn display crystal phases corresponding to lower oxidation states compared to those expected in lithium battery cathode materials [26]. Additionally, diffraction signals of $CaCO_3$ were detected due to the use of metallic Ca as a reducing agent during the mechanochemical treatment. In contrast, the XRD pattern of the MT electrode powder (Fig. 2b) could be confidently matched by patterns of graphite and delithiated $LiNi_{1/3}Co_{1/3}Mn_{1/3}O_2$ (NMC111) structure. This can be explained by observing that the mechanical pretreatment does not involve chemical transformation of the battery electrode powder.

To evaluate the chemical state of metals and carbon contained in TT, MT and MCT, XPS measurements were carried out. The XPS survey spectra of the TT sample (Fig. 2c) display only two main components related to the presence of C and O on the surface of the powder particles, with no significant metal signals detected. In contrast, XPS analysis of the MT sample (Fig. 2d) shows the presence of the expected metals and impurities. To explain the absence of metal signals during the XPS analysis of TT sample, TEM analysis was performed. The TEM image in Fig. S1a of Supporting Information File shows a clear layer of around 8

nm enclosing the metallic particles in a metal-carbon core-shell configuration. The electron diffraction pattern (Fig. S1b) indicates a completely amorphous material. This finding, combined with the XPS results for the TT samples, suggests the presence of amorphous carbon covering the metal particles. Notably, in the present conditions the escape depth of XPS photoelectrons can generally be estimated not to exceed 10 nm, which justifies the predominance of C signals in the XPS spectra of TT at the expenses of the metal ones. The GO yield could be influenced by the oxidation or exfoliation of graphite contained in the EoL LIBs black mass, which may occur during the pretreatment or the battery cycling [15]. In order to investigate the effect of the different pretreatments on graphite, in Fig. 3, the C 1s spectra of TT (Fig. 3a), MT (Fig. 3b) and MCT (Fig. 3c) samples are reported while, for comparison, C 1s spectra of reference pure graphite is reported in Fig. S3a. All samples show a predominant asymmetric signal at 284.05 eV (magenta line) due to the graphitic and amorphous carbon portion of the black mass [27,28], followed by a peak at 284.65 eV (dashed line) attributable to sp3–hybridized C defective sites, typical of high surface area graphitic materials [29]. Unlike the case of pure graphite (Fig. S3a), in TT, MT and MCT (Fig. 3a–c) samples, considerable photoelectron intensity can be detected above 284 eV. These contributions at higher binding energy (BE) are associated to C oxidation species and can be related mainly to three factors: (i) amorphous carbon contained in the EoL LIBs black mass along with graphite and used as conductive additive, which generally contains carbon oxidation groups on the surface, (ii) the oxidation of amorphous carbon or graphite induced by the pretreatment, (iii) the occurrence of carbon or graphite faradaic oxidation reactions during the lifecycle of the battery. These C components can be attributed to epoxy (286.45 eV, yellow) and carboxyl (288.90 eV, green) functionalities, with a faint further contribution from graphitic π-π* shake-up transitions around 291.5 eV [29,30]. The overall ratio $R_{O/C}$ (Eq. S(3)) value is larger for the TT sample (0.21) than for MT (0.13), which is in agreement with
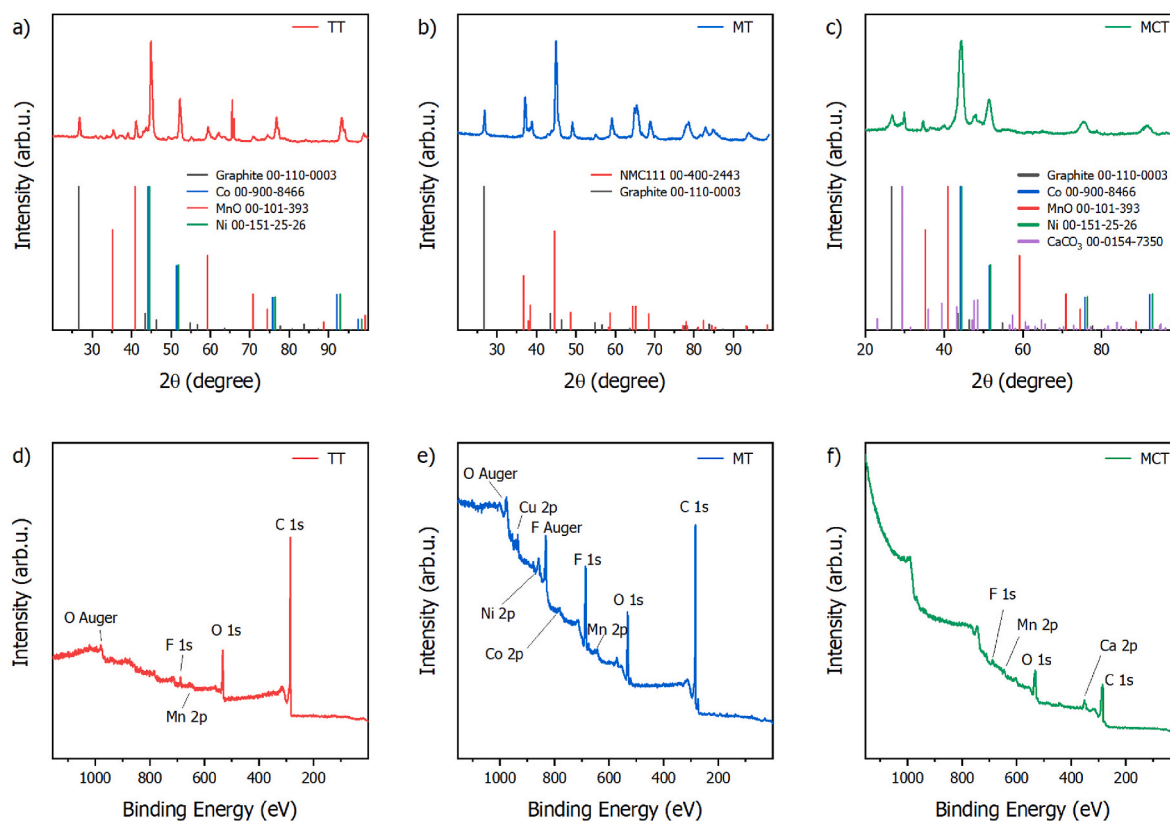
Fig. 2. XRD pattern of black masses obtained after the three different pretreatments, (a) thermally treated (TT), (b) mechanically treated (MT) and (c) mechanochemically treated (MCT). XPS survey spectra of TT (d), MT (e) and MCT (f).
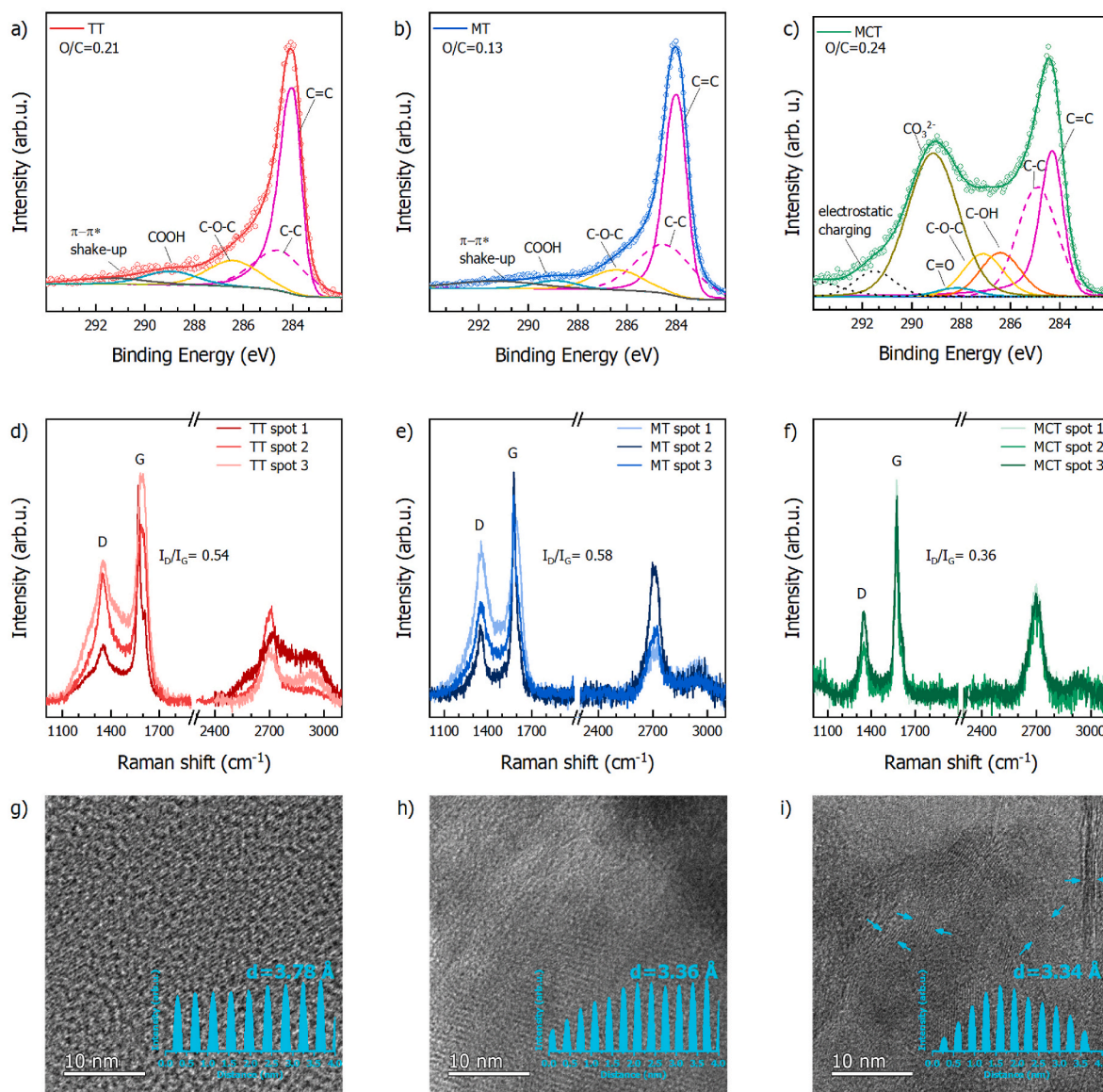
Fig. 3. C 1s XPS spectra of TT (a), MT (b) and MCT (c). Raman spectra recorded for TT (d) MT (e) and MCT (f) in different sample area (spot 1–3). TEM images with inset contrast profiles showing the interlayer spacing of graphite contained in TT (g), MT (h), and MCT (i) samples.

the effects of the thermal treatment on the carbon fraction of the black mass. The C 1s spectrum of MCT sample (Fig. 3c) includes an intense feature at 289.10 eV due to inorganic carbonate. This peak, coupled to the detected Ca signal (Fig. S2), supports the presence of $CaCO_3$ [31], as detected by XRD. The $R_{O/C}$ value (not inclusive of the carbonate contribution) obtained for MCT sample is 0.24, which is higher than TT and MT. In this case, the presence of the $CaCO_3$ feature may have introduced a considerable level of uncertainty in the reconstruction of the experimental XPS spectrum via curve-fitting, which would eventually propagate to the increase of $R_{O/C}$ value. The $R_{O/C}$ value in commercial graphite (Fig. S3a) is very low (0.014), as expected.

TT, MT, MCT and graphite powders were analysed using μ-Raman spectroscopy, and the spectra (Fig. 3d–f) were compared with those of commercial graphite (Fig. S3b). In particular, the Raman spectrum of graphite displays the most prominent signal localized at ≈ 1580 cm^{-1} and known as G band which is due to the C–C stretching vibration of sp^2 C atoms in addition to a weaker D band localized at ≈ 1358 cm^{-1} and attributable to the breathing mode of the sp^2 carbon-rings near the defects [32]. In fact, the intensity of the D band, is sensitive to the structural defects in carbon-based materials and the ratio between the

intensities of the D band and the G band (I_D/I_G) can be utilized as a semi-quantitative parameter to assess the graphitic order of a sample. The I_D/I_G ratio significantly increases in the TT, MT and MCT powders compared to the graphite and there is also a variation of both the shape and position of the G band (Fig. 3d–f). This could be attributed to exfoliation and oxidation occurring during battery usage and/or to the presence of amorphous carbon used as a conductive additive in the battery.

Cell parameters were determined through Rietveld refinement analysis of the experimental patterns shown in Fig. 2a–c and Fig. S4. The estimated cell parameters (Table S1) indicate a slight increase in the lattice parameter c ($P6_3mc$ space group), i.e. graphite layers distance, following the order TT, MT, and MCT. The structures of all samples were further analysed using TEM to directly measure the graphite interlayer spacing. Fig. 3g–i presents TEM images showing cross-sectional views of TT, MT, MCT, and graphite (Fig. S3c), where the layered structures of the graphite contained in each sample are clearly visible through the alternating bright and dark contrasts. Line profiles of contrast intensity across the stacking layers at representative locations are plotted within the corresponding images. The average interlayer spacings were

measured as 3.78 Å for TT, 3.36 Å for MT, 3.36 Å for MCT. TEM indicates that TT exhibits the largest interlayer spacing among all the samples, which can be attributed to the partial oxidation of the graphite present in the electrode powder during the carbothermal reduction process for metal reduction, as evidenced by the XPS $R_{O/C}$ value and the Raman I_D/I_G ratio. The significant increase in interlayer spacing for the TT sample compared to the other samples should result in a substantial shift of the 002 XRD diffraction peak relative to the other samples. However, this shift is not evident likely due to the heterogeneity of the sample and the localized nature of the TEM measurement compared to the bulk analysis provided by XRD. The interlayer spacing for both MT and MCT is nearly identical, consistent with the values expected for EoL graphite [15]. Remarkably, although the MCT sample exhibits the same interlayer spacing as the MT sample, the TEM image of MCT (Fig. 3i) reveals a disordered graphite structure including stacking disorder and delamination (arrows in Fig. 3i), likely resulting from the mechanical exfoliation of graphite induced by the shear forces generated during the ball milling stage of mechanochemical pretreatment [33,34].

3.2. Synthesis of GO via direct application of black mass

TT, MT, MCT were used as graphite source in the Hummers' method obtaining the GOs referred to as TTH, MTH, MCTH, respectively. For comparison, Hummers' method was also applied on commercial graphite (GO referred as graphiteH). The lineshape and $R_{O/C}$ value (0.41) of the C 1s spectrum of graphiteH (Fig. S5) demonstrate the obtainment of GO as a product. In fact, the first main peak can be fitted to a unique component at 284.80 eV, associated to the aromatic C=C network [27,28,35,36] (purple curve, Fig. S5). The oxidized region at higher BE can be fitted to several components, based on the well-known chemical composition of GO in terms of oxygenated functional groups (OFGs), e.g. epoxy and hydroxyl groups on the basal plane, and

carboxylic, carboxylate, carbonyl (ketones, quinones), phenol, ester and lactone groups at edges and defects [37]. Therefore, the proposed curve-fitting in the oxidized area involves two components centered at 286.55 eV (red) and 287.05 eV (yellow), usually assigned to hydroxyl and epoxy groups, while two further components at 288.05 (cyan) and 289.05 eV (grey) can respectively be assigned to carbonyl (ketones, quinones) and carboxyl (esters, lactones, carboxylic acids) groups [38–40]. The C 1s XPS spectra of the corresponding TTH, MTH and MCTH materials (Fig. 4a–c) display a lineshape similar to that of graphiteH (Fig. S5), though with a less pronounced intensity in the OFG area. In fact, the sum of epoxy and hydroxyl components results in a minor relative amount of the corresponding OFGs (30.5, 26.0 and 23.4 % for TTH, MTH and MCTH, respectively) than for graphiteH (31.9 %), suggesting that in these samples the Hummers' reactions occurred less efficaciously (see Table S3).

Raman spectra (Fig. 4d) confirm the production of GO sheets that display the characteristic D band -localized at ≈1358 cm^{-1} and with a I_D/I_G ratio equal to 0.76 for graphiteH and0.80, 0.84 and 0.83 for MTH, TTH and MCTH, respectively. XRD spectra illustrating the crystal structures of the GO samples are reported in Fig. 4e. It is apparent that the Hummer's method leaves only minimal residual diffraction features of the original graphite samples (Fig. S4 and Fig. 2a–c), demonstrating the effective disruption of the graphite crystal structure. The primary 002 reflection, typically observed at a 2θ value of approximately 26.7° for graphite, appears with very low intensity when detected. Notably, also the characteristic 001 peak, commonly reported at 2θ values of 10–12° for GO in the literature [41], is observed with very low intensity for MCTH and MTH, absent in TTH, and most prominent in graphiteH. The diminished or absent 001 peak indicates the lack of a stacked layer structure, likely due to the extremely small size and highly disrupted arrangement of the GO sheets [42] obtained from the black masses if compared with commercial graphite. Furthermore, the 001 peak is
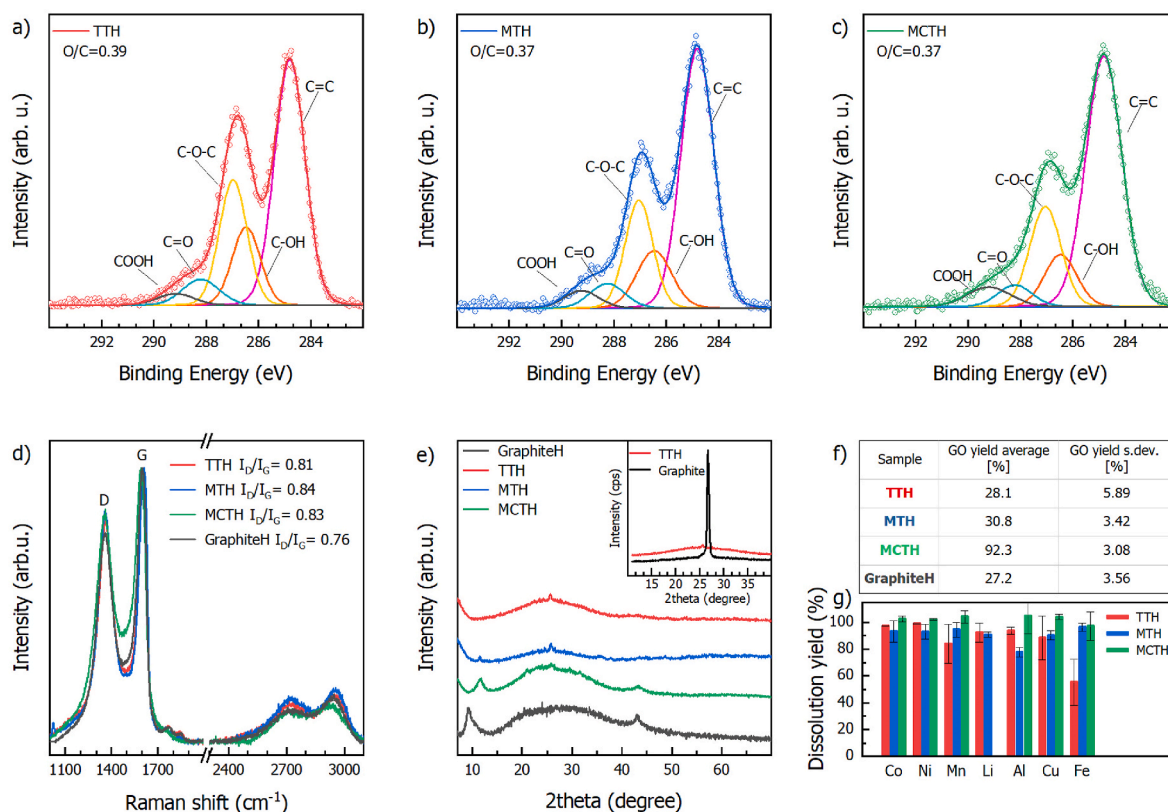
Fig. 4. C 1s XPS spectra of samples prepared using Hummers' method: TTH (a), MTH (b), and graphiteH (c). Raman spectra (d) and XRD patterns (e) for TTH, MTH, MCTH and graphiteH. The inset in the XRD patterns shows the unnormalized patterns for TTH and graphite. (f) GO yields and metal dissolution yields obtained using Hummers' method.

clearly observed in the residual graphite oxides isolated by centrifugation from GOs (Fig. S6), highlighting the effectiveness of the isolation method in separating graphite oxide from exfoliated GO.

The results of GO production and metal extraction by direct application of the Hummers' method are reported in Fig. 4f and g, respectively. For recycling purposes, it is crucial to recover the metals, as this improves the overall efficiency of the process. In Fig. 4g, metal dissolution yields are reported, showing that, for each black mass, the Hummers' method enables the quantitative extraction of all the metals. Slight differences can be observed in the dissolution yields of Fe, Cu, and Al. In fact, these metals are present in low concentrations in the original black masses and mainly originate from current collectors and battery cases. Therefore, they are present with different granulometry compared to the active materials, leading to heterogeneity in their concentration in the treated samples. In Fig. 4f, GO yields computed by Eq. S(1) are reported to evaluate the effect of pretreatment on GO production. No significant differences between the GO yields achieved by employing TT and MT black masses, and graphite. For each of these materials, a GO yield around 30 % is found. In contrast, a remarkably high GO yield of 92 % is observed for MCTH, highlighting that the mechanochemical pretreatment promotes partial exfoliation of graphite, resulting in graphite stacks with fewer layers, as evidenced by the TEM images (Fig. 3i). Additionally, the ball milling treatment performed during the mechanochemical pretreatment induces a reduction in particle size. MCT particles exhibit a size distribution with a D90 of 10 μm, whereas TT and MT particles have D90 values of 210 μm and 129 μm, respectively (Fig. S7). The smaller size of the MCT particles enhances mass transfer, which has been reported to control the reaction efficiency in the Hummers' method, thereby increasing the oxidation yield [43].

3.3. Synthesis of GO after acid leaching

To evaluate whether the presence of the metals contained in the black masses could influence the conversion of graphite to GO, the Hummers' method was replicated by employing the graphite left after metal dissolution. To this purpose, leaching was carried out using H_2SO_4 and H_2O_2 by employing TT, MT, MCT and commercial graphite (graphite materials produced are hereafter referred to as TTL, MTL, MCTL, and graphiteL, respectively). Characterization of the obtained graphite materials was conducted to assess the occurrence of oxidation or exfoliation, which has been reported to take place during the leaching with H_2SO_4 and H_2O_2[15]. The leaching with the commercial graphite produced significant changes in the chemical composition (Fig. S8). Specifically, an increase in the C 1s XPS intensity is observed for the graphiteL within the range of oxidized carbon contributions, above ~285 eV. The raw C 1s spectrum can be deconvoluted into features corresponding to C–OH, C=O, and COOH functional groups, likely originating from the oxidative action of the H_2SO_4– H_2O_2 mixture, resulting in an $R_{O/C}$ ratio of 0.18, approximately 13 times higher than that of pristine commercial graphite (Fig. S3a). This effect is also evident in the C 1s XPS spectra of TTL, MTL and MCTL samples (Fig. 5a–c). In this case, the leaching of the black mass samples also leads to an increase in the concentration of oxygenated functional groups, with $R_{O/C}$ ratios of 0.26, 0.32, and 0.25 for TTL, MTL, and MCTL, respectively (Table S3). In the MTL sample, a contribution from CF_2 groups at 290.9 eV is also observed, likely originating from residual PVDF content in the corresponding black mass. The presence of defects in the carbon-based materials due to the leaching processes was also proved through Raman spectroscopy.

Specifically, the I_D/I_G ratio in the graphite spectrum notably increases from 0.04 (Fig. S3b) in the commercial powder to 0.14 after performing the leaching (Fig. 5d, black line). As expected, the introduction of defects as a result of leaching also occurs in all three black masses, independently from their preparation procedures as proved by their Raman spectra (Fig. 5a). In particular, in the spectra of TTL, MTL, and MCTL samples, the I_D/I_G ratio compared to the respective spectra of
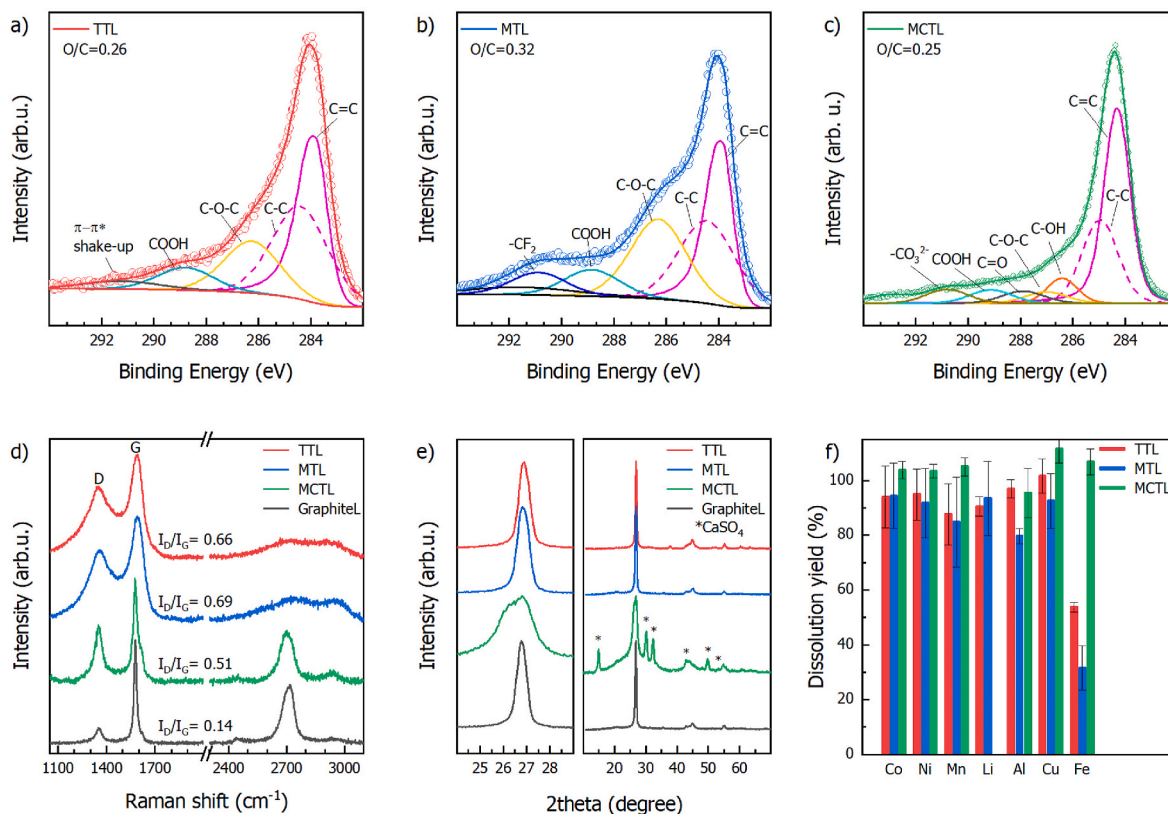
Fig. 5. C 1s XPS spectra of samples after acid leaching performed using 1.5 M H_2SO_4 and 15 % v/v H_2O_2. (a) TTL, (b) MTL, and (c) MCTL. Raman spectra (d), XRD patterns (e), and (f) metal dissolution yields achieved through acid leaching.

the pristine powders (Fig. 3d–e) sensibly increased. Concerning the MCTL sample, XPS analysis seems to contradict Raman: the $R_{O/C}$ calculated through XPS remains almost the same (0.24 in MCT *vs.* 0.25 in MCTL), while the defects evaluated with the Raman increase. This apparent contradiction could be attributed to the relevant presence of CO_3^{2-} ions in the MCT sample, which are no longer present after leaching. Fig. 5e presents the XRD data of samples after acid treatment. It is evident that all patterns are qualitatively identical and correspond to the unique phase of pure graphite, with the exception of MCTL. For TTL, MTL and graphite, the interlayer spacing d_{002} after acid leaching corresponds to 3.32, 3.32 and 3.33 Å with no significative variation with respect to the pristine sample. In the XRD pattern of MCTL, additional peaks are observed, attributed to $CaSO_4$, which forms as a result of the reaction between $CaCO_3$ and $Ca(OH)_2$ (originally present in MCT) with H_2SO_4. The presence of sulphate and $CaSO_4$ was further confirmed by the XPS wide spectrum (Fig. S9). Notably, the 002 peak for graphite in MCTL appears asymmetrically broadened and shifted toward lower angles, with reduced sharpness and an increase in the amorphous halo beneath the 002 reflection is observed (Fig. 5e). These observations indicate a reduction in stacking order and suggest a potential increase in the amorphous phase. Furthermore, the interlayer spacing of the 002 reflection slightly increases up to 3.35 Å in MCTL (Table S2). These findings suggest that acid leaching promotes the oxidation and exfoliation of graphite in MCT to a greater exent compared to the other black masses.

TTL, MTL, MCTL and graphiteL (previously leached TT, MT, MCT and graphite samples) were then used as starting materials in the Hummers' method. The C 1s XPS spectra of the produced solids (Fig. 6a–c and Fig. S10) show the characteristic features of GO, similarly to those reported in Fig. 4. A close comparison of TTLH, MTLH and MCTLH with their corresponding non-leached analogues (TTH. MTH and MCTH) shows that the overall $R_{O/C}$ is not affected by leaching

(Table S3). Likewise, when Hummer's protocol is performed on the previously leached black masses and leached commercial graphite, layers of GO with comparable density of defects are obtained, as proved by Raman spectra (Fig. 6d). Moreover, Fig. 6-e shows the XRD patterns of samples after both acid leaching and subsequent Hummers' treatment. The patterns are similar to those reported for GO obtained via the Hummers' method (Fig. 4e). However, the 001 peak, clearly observed in commercial graphite after the Hummers' method (Fig. 4e), is not present in this case, confirming the effectiveness of acid leaching in initiating the oxidation and facilitating the subsequent exfoliation of graphite.

3.4. Discussion on GO yields

Comparing the GO yield results obtained from the two investigated routes, i.e. application of Hummers' method directly on the black mass (route 1 - Fig. 4f) and after acid leaching (route 2 - Fig. 6f), the following consideration can be inferred.

- The metals present in the black masses consume Hummers' reagents $KMnO_4$, H_2SO_4 and H_2O_2. Metals contained in MCT black mass originating from cathode materials such as $LiMO_2$ (where M represents Co, Ni, Mn, or their mixed oxides, with an oxidation state higher than +2) interact with H_2SO_4 and H_2O_2. H_2SO_4 acts as a proton source to break metal-oxide bonds, leading to the formation of oxygen and water, while H_2O_2 serves as a reducing agent. In the case of pretreatment procedures that involves the chemical reduction of the transition metals originally present in the cathode materials (TT and MCT), H_2SO_4, $KMnO_4$, and H_2O_2 may also be consumed as oxidizing agents.
- Conventional acid leaching appears to positively influence the GO yield, not only through metal removal but also by enhancing the yield itself. This is demonstrated by the increase in GO yield observed
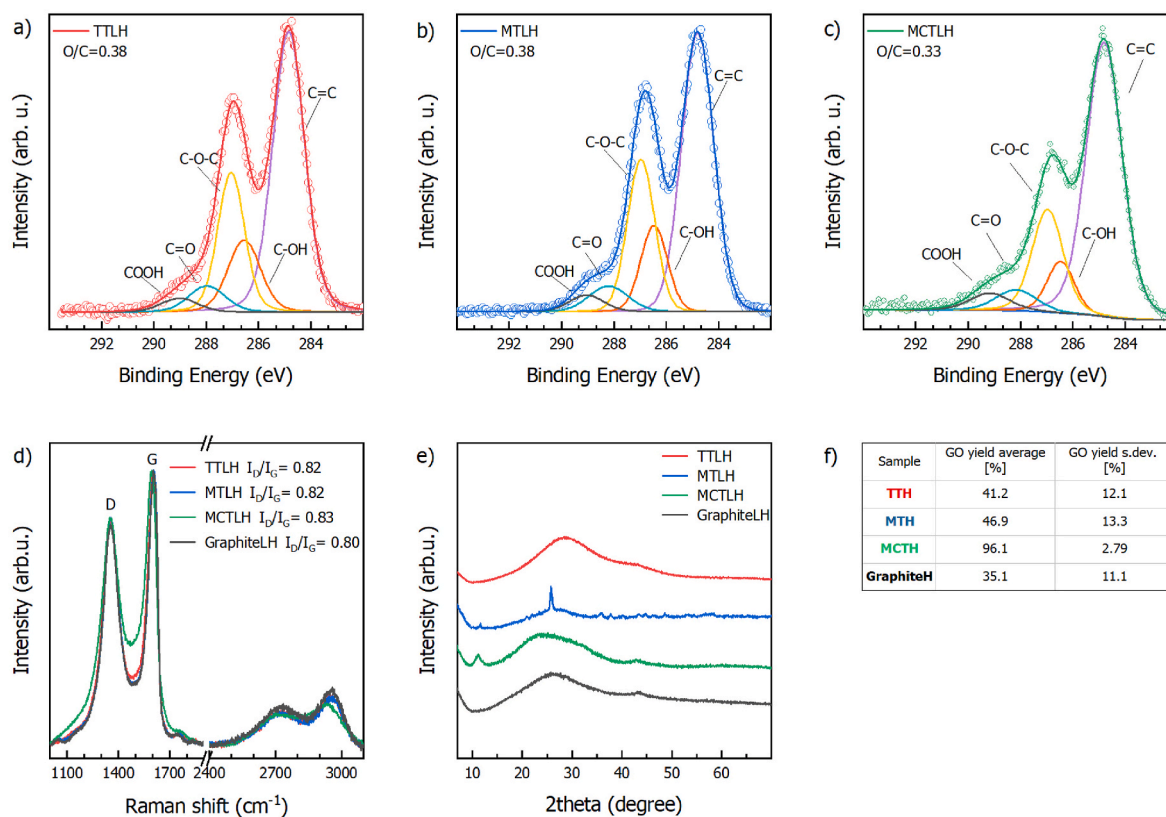

Fig. 6. C 1s XPS spectra of GO obtained by applying Hummers' method after acid leaching performed to remove the metals TTLH (a), MTLH (b) and MCTLH (c). Raman spectra (d) and XRD patterns (e) recorded for TTLH, MTLH and MCTLH. (f) GO yields.

in commercial graphite (which naturally contains no metals), where the GO yield rises from 27 % when Hummers' method is applied directly to graphite, to 35 % when it is applied after acid leaching. The effect of leaching is further confirmed by the increased $R_{O/C}$ value after leaching (Fig. 5a–c, Fig. S8) and by higher defectivity, as evidenced by Raman measurements (Fig. 5d), when compared to pristine black masses and commercial graphite.

- Pretreatments may primarily involve metals with different oxidation states, leading to variable consumption of Hummers' reagents, but they could also involve mechanical or oxidative exfoliation. The MCT powder, subjected to ball milling, exhibits the highest GO yield among all the samples. When using Hummers' method alone the GO yield was 92 %, whereas applying the Hummers' method after acid leaching increased the yield to 96 %. The highest GO yield obtained via route 1 can be attributed to the exfoliation of graphite caused by the forces generated during ball milling, which is part of the mechanochemical pretreatment. This process also reduces the graphite particle size, thereby enhancing mass transfer during the Hummers' reactions [43]. The observed increase in GO yield after metal removal (MCTLH) can be attributed to the improved efficiency of the Hummers' method. In the MCT sample, the black mass contains $CaCO_3$ and $Ca(OH)_2$ due to the reduction reaction with metallic Ca. These compounds may lead to greater consumption of Hummers' reagents. Acid leaching neutralizes $CaCO_3$ and $Ca(OH)_2$, thereby reducing reagent consumption in the following Hummers method and contributing to the observed increase in GO yield.

- The impact of employing the graphite from EoL LIBs rather than pristine graphite is clearly evident in the GO yield obtained via route 2. Specifically, the GO yield of graphiteLH is the lowest observed, even lower than that of the MTLH sample where chemical oxidation or significant mechanical exfoliation during pretreatment can be excluded. The higher GO yield for MTLH can be directly attributed to the EoL graphite content. Moreover, it is worth noting that the leaching effect on graphite is expected to be more pronounced in the case of commercial graphite with respect to black masses. For commercial graphite, leaching reagents are fully available for oxidation and exfoliation while, in black masses, these reagents are also consumed in the reaction with metals from cathode materials and other components. The higher GO yield for all black masses compared to graphiteLH is likely due to lithium intercalation/deintercalation and faradaic oxidation processes occurring during the battery's lifecycle, which partially exfoliate and oxidize the graphite [15].

4. Conclusion

This study demonstrates the impact of various pretreatment methods on the synthesis of GO from black masses recovered from EoL LIBs. Two synthesis routes were explored: application of the Hummers' method directly to black mass and after an acid leaching procedure, typically used in LIB recycling for metal extraction. Among the pretreatments, mechanochemical treatment yielded the highest GO production, with a 92 % yield after direct Hummers' method application and 96 % after acid leaching. This improvement is attributed to exfoliation and particle size reduction caused by ball milling, which enhances mass transfer during the GO synthesis reaction. It was found that GO yields increased after metal removal from the black masses, as metals consume Hummers' reagents. Moreover, acid leaching introduced oxygen functional groups that facilitated further graphite exfoliation, improving the GO yields. The study also demonstrated that graphite from EoL LIBs, yielded higher GO compared to commercial graphite, due to partial exfoliation and oxidation promoted by lithium intercalation/deintercalation and faradaic oxidation processes occurring during the battery's lifecycle. Overall, these findings underscore the potential of combining mechanochemical treatment and acid leaching to enhance GO production in LIB recycling, highlighting the importance of selecting appropriate pre-

treatment strategies for efficient and sustainable high-value product recovery. Additionally, the reported GO yields provide valuable data for assessing the scalability of the proposed method on a larger scale.

CRediT authorship contribution statement

Pier Giorgio Schiavi: Writing – review & editing, Writing – original draft, Validation, Supervision, Methodology, Investigation, Funding acquisition, Formal analysis, Data curation, Conceptualization. **Ludovica D'Annibale:** Methodology, Investigation, Data curation. **Andrea Giacomo Marrani:** Writing – review & editing, Writing – original draft, Methodology, Investigation, Data curation. **Francesco Amato:** Methodology, Investigation, Data curation. **Olga Russina:** Methodology, Data curation. **Silvia Iacobelli:** Methodology. **Francesco Mura:** Methodology. **Raphael Sieweck:** Methodology. **Francesca Pagnanelli:** Visualization, Supervision. **Pietro Altimari:** Writing – review & editing, Supervision, Project administration, Funding acquisition.

Declaration of competing interest

The authors declare that they have no known competing financial interests or personal relationships that could have appeared to influence the work reported in this paper.

Acknowledgments

Appendix A. Supplementary data

Supplementary data to this article can be found online at https://doi.org/10.1016/j.carbon.2025.120295.

References

[1] J.C.Y. Jung, P.C. Sui, J. Zhang, A review of recycling spent lithium-ion battery cathode materials using hydrometallurgical treatments, J. Energy Storage 35 (2021) 102217, https://doi.org/10.1016/J.EST.2020.102217.

[2] S. Kim, J. Bang, J. Yoo, et al., A comprehensive review on the pretreatment process in lithium-ion battery recycling, J. Clean. Prod. 294 (2021) 126329, https://doi.org/10.1016/J.JCLEPRO.2021.126329.

[3] Z. Yan, A. Sattar, Z. Li, Priority Lithium recovery from spent Li-ion batteries via carbothermal reduction with water leaching, Resour. Conserv. Recycl. 192 (2023) 106937, https://doi.org/10.1016/J.RESCONREC.2023.106937.

[4] G. Zhang, X. Yuan, C.Y. Tay, Y. He, H. Wang, C. Duan, Selective recycling of lithium from spent lithium-ion batteries by carbothermal reduction combined with multistage leaching, Sep. Purif. Technol. 314 (2023) 123555, https://doi.org/10.1016/J.SEPPUR.2023.123555.

[5] J. Li, Y. Tian, B. Yang, B. Xu, J. Hu, S. Yao, A process for preferential recovery of lithium and manganese from spent NCM by vacuum carbothermal reduction method, Sep. Purif. Technol. 354 (2025) 129035, https://doi.org/10.1016/J.SEPPUR.2024.129035.

[6] O. Dolotko, N. Gehrke, T. Malliaridou, et al., Universal and efficient extraction of lithium for lithium-ion battery recycling using mechanochemistry, Commun. Chem. 6 (1) (2023) 49, https://doi.org/10.1038/s42004-023-00844-2.

[7] M. Wang, K. Liu, J. Yu, C.C. Zhang, Z. Zhang, Q. Tan, Recycling spent lithium-ion batteries using a mechanochemical approach, Circular Economy 1 (2) (2022) 100012, https://doi.org/10.1016/J.CEC.2022.100012.

[8] C. Xing, M. Yao, L. Fei, Upcycling degraded layered oxide cathodes from spent lithium-ion batteries toward emerging materials: a review, Energy Storage Mater. 71 (2024) 103636, https://doi.org/10.1016/J.ENSM.2024.103636.

[9] M. Abdollahifar, S. Doose, H. Cavers, A. Kwade, Graphite recycling from end-of-life lithium-ion batteries: processes and applications, Adv Mater Technol 8 (2) (2023) 2200368, https://doi.org/10.1002/ADMT.202200368.

[10] H. Tian, M. Graczyk-Zajac, A. Kessler, A. Weidenkaff, R. Riedel, Recycling and reusing of graphite from retired lithium-ion batteries: a review, Adv. Mater. 36 (13) (2024) 2308494, https://doi.org/10.1002/ADMA.202308494.

[11] F. Farjadian, S. Abbaspour, M. Amin, et al., Recent developments in graphene and graphene oxide: properties, synthesis, and modifications: a review,

ChemistrySelect 5 (33) (2020) 10200–10219, https://doi.org/10.1002/SLCT.202002501.

[12] Schiavi PG, Zanoni R, Branchi M, et al. Upcycling real waste mixed lithium-ion batteries by simultaneous production of rGO and lithium-manganese-rich cathode material. ACS Sustain Chem Eng. 9(39):13303-13311. doi:10.1021/acssuschemeng.1c04690.

[13] K. He, Z.Y. Zhang, F.S. Zhang, Synthesis of graphene and recovery of lithium from lithiated graphite of spent Li-ion battery, Waste Management 124 (2021) 283–292, https://doi.org/10.1016/J.WASMAN.2021.01.017.

[14] P. Nazari, A. Hamidi, R. Golmohammadzadeh, F. Rashchi, E. Vahidi, Upcycling spent graphite in LIBs into battery-grade graphene: managing the produced waste and environmental impacts analysis, Waste Management 174 (2024) 140–152, https://doi.org/10.1016/J.WASMAN.2023.11.038.

[15] Y. Zhang, N. Song, J. He, R. Chen, X. Li, Lithiation-aided conversion of end-of-life lithium-ion battery anodes to high-quality graphene and graphene oxide, Nano Lett. 19 (1) (2019) 512–519, https://doi.org/10.1021/acs.nanolett.8b04410.

[16] W. Zhang, Z. Liu, J. Xia, et al., Preparing graphene from anode graphite of spent lithium-ion batteries, Front. Environ. Sci. Eng. 11 (5) (2017) 1–8, https://doi.org/10.1007/S11783-017-0993-8/METRICS.

[17] J. Yu, M. Lin, Q. Tan, J. Li, High-value utilization of graphite electrodes in spent lithium-ion batteries: from 3D waste graphite to 2D graphene oxide, J. Hazard Mater. 401 (2021) 123715, https://doi.org/10.1016/J.JHAZMAT.2020.123715.

[18] L. Yang, L. Yang, G. Xu, et al., Separation and recovery of carbon powder in anodes from spent lithium-ion batteries to synthesize graphene, Sci. Rep. 9 (1) (2019) 1–7, https://doi.org/10.1038/s41598-019-46393-4, 2019 9:1.

[19] S. Natarajan, Ede S. Rao, H.C. Bajaj, S. Kundu, Environmental benign synthesis of reduced graphene oxide (rGO) from spent lithium-ion batteries graphite and its application in supercapacitor, Colloids Surf. A Physicochem. Eng. Asp. 543 (2018) 98–108, https://doi.org/10.1016/J.COLSURFA.2018.01.054.

[20] S. Natarajan, H.C. Bajaj, V. Aravindan, Template-free synthesis of carbon hollow spheres and reduced graphene oxide from spent lithium-ion batteries towards efficient gas storage, J Mater Chem A Mater 7 (7) (2019) 3244–3252, https://doi.org/10.1039/C8TA11521D.

[21] D. Ruan, Z. Zhang, X. Wu, et al., Synthesizing high-quality graphene from spent anode graphite and further functionalization applying in ORR electrocatalyst, ChemistrySelect 6 (1) (2021) 90–95, https://doi.org/10.1002/SLCT.202004230.

[22] J.S. Ribeiro, M.B.J.G. Freitas, J.C.C. Freitas, Recycling of graphite and metals from spent Li-ion batteries aiming the production of graphene/CoO-based electrochemical sensors, J. Environ. Chem. Eng. 9 (1) (2021) 104689, https://doi.org/10.1016/J.JECE.2020.104689.

[23] K. Liivand, M. Kazemi, P. Walke, et al., Spent Li-ion battery graphite turned into valuable and active catalyst for electrochemical oxygen reduction, ChemSusChem 14 (4) (2021) 1103–1111, https://doi.org/10.1002/CSSC.202002742.

[24] L. Yang, L. Yang, G. Xu, et al., Separation and recovery of carbon powder in anodes from spent lithium-ion batteries to synthesize graphene, Sci. Rep. 9 (1) (2019) 1–7, https://doi.org/10.1038/S41598-019-46393-4/TABLES/2.

[25] G. Zhang, X. Yuan, C.Y. Tay, Y. He, H. Wang, C. Duan, Selective recycling of lithium from spent lithium-ion batteries by carbothermal reduction combined with multistage leaching, Sep. Purif. Technol. 314 (2023) 123555, https://doi.org/10.1016/J.SEPPUR.2023.123555.

[26] O. Dolotko, N. Gehrke, M. Knapp, H. Ehrenberg, Mechanochemically induced hydrometallurgical method for recycling d-elements from Li-ion battery cathodes, J. Alloys Compd. 976 (2024) 172884, https://doi.org/10.1016/J.JALLCOM.2023.172884.

[27] G. Speranza, L. Minati, The surface and bulk core lines in crystalline and disordered polycrystalline graphite, Surf. Sci. 600 (19) (2006) 4438–4444, https://doi.org/10.1016/J.SUSC.2006.07.008.

[28] M.R.C. Hunt, Surface and bulk components in angle-resolved core-level photoemission spectroscopy of graphite, Phys Rev B Condens Matter Mater Phys 78 (15) (2008), https://doi.org/10.1103/PHYSREVB.78.153408/FIGURES/2/THUMBNAIL.

[29] H. Estrade-Szwarckopf, XPS photoemission in carbonaceous materials: a "defect" peak beside the graphitic asymmetric peak, Carbon N Y 42 (8–9) (2004) 1713–1721, https://doi.org/10.1016/J.CARBON.2004.03.005.

[30] A. Barinov, O.B. Malcioğlu, S. Fabris, et al., Initial stages of oxidation on graphitic surfaces: photoemission study and density functional theory calculations, J. Phys. Chem. C 113 (21) (2009) 9009–9013, https://doi.org/10.1021/JP902051D/ASSET/IMAGES/MEDIUM/JP-2009-02051D_0005.GIF.

[31] M. Ni, B.D. Ratner, Differentiating calcium carbonate polymorphs by surface analysis techniques—an XPS and TOF-SIMS study, Surf. Interface Anal. 40 (10) (2008) 1356–1361, https://doi.org/10.1002/SIA.2904.

[32] A.G. Marrani, A.C. Coico, D. Giacco, et al., Integration of graphene onto silicon through electrochemical reduction of graphene oxide layers in non-aqueous medium, Appl. Surf. Sci. 445 (2018) 404–414.

[33] J.Y. Huang, HRTEM and EELS studies of defects structure and amorphous-like graphite induced by ball-milling, Acta Mater. 47 (6) (1999) 1801–1808, https://doi.org/10.1016/S1359-6454(99)00067-1.

[34] M. Yi, Z. Shen, A review on mechanical exfoliation for the scalable production of graphene, J Mater Chem A Mater 3 (22) (2015) 11700–11715, https://doi.org/10.1039/C5TA00252D.

[35] F. Amato, I. Ferrari, A. Motta, R. Zanoni, E.A. Dalchiele, A.G. Marrani, Assessing the evolution of oxygenated functional groups on the graphene oxide surface upon mild thermal annealing in water, RSC Adv. 13 (42) (2023) 29308–29315, https://doi.org/10.1039/D3RA05083A.

[36] F. Amato, G. Perini, G. Friggeri, et al., Unlocking the stability of reduced graphene oxide nanosheets in biological media via use of sodium ascorbate, Adv Mater Interfaces 10 (22) (2023) 2300105, https://doi.org/10.1002/ADMI.202300105.

[37] P.P. Brisebois, M. Siaj, Harvesting graphene oxide – years 1859 to 2019: a review of its structure, synthesis, properties and exfoliation, J Mater Chem C Mater 8 (5) (2020) 1517–1547, https://doi.org/10.1039/C9TC03251G.

[38] V. Palmieri, F. Amato, A.G. Marrani, et al., Graphene oxide-mediated copper reduction allows comparative evaluation of oxygenated reactive residues exposure on the materials surface in a simple one-step method, Appl. Surf. Sci. 615 (2023) 156315, https://doi.org/10.1016/J.APSUSC.2022.156315.

[39] R. Larciprete, P. Lacovig, S. Gardonio, A. Baraldi, S. Lizzit, Atomic oxygen on graphite: chemical characterization and thermal reduction, J. Phys. Chem. C 116 (18) (2012) 9900–9908, https://doi.org/10.1021/JP2098153/SUPPL_FILE/JP2098153_SI_001. PDF.

[40] F. Amato, A. Motta, L. Giaccari, et al., One-pot carboxyl enrichment fosters water-dispersibility of reduced graphene oxide: a combined experimental and theoretical assessment, Nanoscale Adv. 5 (3) (2023) 893–906, https://doi.org/10.1039/D2NA00771A.

[41] X. Jiao, Y. Qiu, L. Zhang, X. Zhang, Comparison of the characteristic properties of reduced graphene oxides synthesized from natural graphites with different graphitization degrees, RSC Adv. 7 (82) (2017) 52337–52344, https://doi.org/10.1039/C7RA10809E.

[42] L. Zhang, J. Liang, Y. Huang, Y. Ma, Y. Wang, Y. Chen, Size-controlled synthesis of graphene oxide sheets on a large scale using chemical exfoliation, Carbon N Y 47 (14) (2009) 3365–3368, https://doi.org/10.1016/J.CARBON.2009.07.045.

[43] A.M. Dimiev, J.M. Tour, Mechanism of graphene oxide formation, ACS Nano 8 (3) (2014) 3060–3068, https://doi.org/10.1021/NN500606A/SUPPL_FILE/NN500606A_SI_001. PDF.